

Article

3D Printed Voltammetric Sensor Modified with an Fe(III)-Cluster for the Enzyme-Free Determination of Glucose in Sweat

Eleni Koukouviti ¹, Alexios K. Plessas ², Anastasios Economou ¹, Nikolaos Thomaidis ¹,
Giannis S. Papaefstathiou ² and Christos Kokkinos ^{1,*}

¹ Laboratory of Analytical Chemistry, Department of Chemistry, National and Kapodistrian University of Athens, 15771 Athens, Greece

² Laboratory of Inorganic Chemistry, Department of Chemistry, National and Kapodistrian University of Athens, 15771 Athens, Greece

* Correspondence: christok@chem.uoa.gr; Tel.: +30-2107274312

Abstract: In this work, a 3D printed sensor modified with a water-stable complex of Fe(III) basic benzoate is presented for the voltammetric detection of glucose (GLU) in acidic epidermal skin conditions. The GLU sensor was produced by the drop-casting of Fe(III)-cluster ethanolic mixture on the surface of a 3D printed electrode fabricated by a carbon black loaded polylactic acid filament. The oxidation of GLU was electrocatalyzed by Fe(III), which was electrochemically generated in-situ by the Fe(III)-cluster precursor. The GLU determination was carried out by differential pulse voltammetry without the interference from common electroactive metabolites presented in sweat (such as urea, uric acid, and lactic acid), offering a limit of detection of 4.3 $\mu\text{mol L}^{-1}$. The exceptional electrochemical performance of $[\text{Fe}_3\text{O}(\text{PhCO}_2)_6(\text{H}_2\text{O})_3]\cdot\text{PhCO}_2$ combined with 3D printing technology forms an innovative and low-cost enzyme-free sensor suitable for noninvasive applications, opening the way for integrated 3D printed wearable biodevices.

Keywords: glucose; 3D printing; sensor; nonenzymatic; voltammetry; iron



Citation: Koukouviti, E.; Plessas, A.K.; Economou, A.; Thomaidis, N.; Papaefstathiou, G.S.; Kokkinos, C. 3D Printed Voltammetric Sensor Modified with an Fe(III)-Cluster for the Enzyme-Free Determination of Glucose in Sweat. *Biosensors* **2022**, *12*, 1156. <https://doi.org/10.3390/bios12121156>

Received: 16 October 2022

Accepted: 9 December 2022

Published: 11 December 2022

Publisher's Note: MDPI stays neutral with regard to jurisdictional claims in published maps and institutional affiliations.



Copyright: © 2022 by the authors. Licensee MDPI, Basel, Switzerland. This article is an open access article distributed under the terms and conditions of the Creative Commons Attribution (CC BY) license (<https://creativecommons.org/licenses/by/4.0/>).

1. Introduction

Diabetes is one of the most common worldwide diseases. It affects millions of individuals, causing serious damage to the nerves and blood vessels, and ranks among the leading causes of death globally [1]. The periodical checking of blood glucose (GLU) levels throughout the day is of vital significance for diabetic patients, which is typically operated via electrochemical self-testing devices based on blood sampling from the patient's fingertip. However, this painful blood sampling discourages the patients from frequent measurements during the daylight, while the tests at night-time are practically neglected. On the contrary, noninvasive GLU monitoring is an ideal route toward calm and painless glucose testing, and fortunately modern electrochemical devices have been introduced for GLU monitoring in sweat, as this epidermal biofluid contains GLU at quantities that correlate well with blood [2–5].

Electrochemical GLU sensors can be split into enzymatic-based and nonenzymatic sensors [6–8]. Typical enzymatic GLU biosensors are based on glucose oxidase (GOx) catalyzing the oxidation of glucose to gluconolactone and producing the by-product hydrogen peroxide, which is amperometrically determined by the sensor. The main problems on the construction of enzymatic GLU biosensors are the efficiency of GOx immobilization on the electrode surface, the presence of dissolved oxygen, and the effect of temperature, pH, and ionic strength on the enzyme activity [9–12]. To overcome these disadvantages, enzyme-free GLU sensors based on metallic particles have been applied as catalysts of GLU electrooxidation, including metals (i.e., Au, Pd and Pt), and metal oxides (i.e., CuO,

Cu₂O, NiO, TiO₂, Co₃O₄, MnO₂, Fe₂O₃ and Fe₃O₄) [13–26], thanks to their high sensitivity, stability and fast response. Nevertheless, these metallic candidates for enzyme-free GLU monitoring usually demonstrate electrocatalytic activity in neutral and basic media and, thus, their applicability in an acidic epidermal skin environment is limited [13–32]. More specifically, regarding the iron-based sensors Fe₃O₄, Fe₂O₃, and FeOOH particles have been used as electrode modifiers for the electrooxidation of GLU in a pH of 7, 7.5, and 13 [27–32].

In this work, we have synthesized a water-insoluble Fe(III)-cluster (iron(III) basic benzoate, [Fe₃O(PhCO₂)₆(H₂O)₃]·PhCO₂) and tested it as an electrode modifier for the enzyme-free, differential pulse voltammetric (DPV) determination of GLU in artificial sweat. The GLU sensor was fabricated using a 3D printed electrode printed from a carbon black loaded polylactic acid (PLA) filament, and the Fe(III)-cluster as ethanolic mixture is drop-casted on the surface of the electrode, followed by its trapping with a Nafion film. The 3D printed sensor was compared with a respective electrode modified with iron oxide that presented poor electrocatalytic ability towards the GLU oxidation in the acidic environment prevailing in epidermal sweat. The cluster of iron (III) basic benzoate exhibited favorable electroanalytical behavior, and once it has been conjugated with 3D printing technology, it leads to an innovative, stable, selective, and sensitive GLU sensor. The core advantages of the presented sensor is its ability to operate in acidic conditions (in contrast to other metallic electrocatalytic GLU sensors), establishing it as suitable for noninvasive applications, while the use of 3D printing overcomes the fabrication disadvantages of manufacturing technologies used in conventional sensors (i.e., screen printed, sputtering), offering low-cost desktop equipment, ease of operation, and fast fabrication and delivery speed with negligible produced waste [33–36].

2. Materials and Methods

2.1. Reagents

All reagents were obtained from Sigma-Aldrich (St. Louis, MO, USA). A stock solution of 0.1 mol L⁻¹ GLU was prepared in water and left for 24 h at room temperature to allow equilibration of the isomers, and stored at 4 °C. The artificial sweat was composed of 3 mmol L⁻¹ NH₄Cl, 50 μmol L⁻¹ MgCl₂, 0.4 mmol L⁻¹ CaCl₂, 80 mmol L⁻¹ NaCl, 8 mmol L⁻¹ KCl, 25 μmol L⁻¹ uric acid, 22 mmol L⁻¹ urea, and 5.5 mmol L⁻¹ lactic acid (pH 4) [12]. The phosphate buffer (PB) was prepared by mixing proper quantities of Na₂HPO₄ and NaH₂PO₄, and the pH value was adjusted to 4 with 1 mol L⁻¹ solution of HCl.

2.2. Synthesis of [Fe₃O(PhCO₂)₆(H₂O)₃]·PhCO₂

Following a typical procedure [37], 5.41 g of FeCl₃·6H₂O (20 mmol) were dissolved in 25 mL H₂O and the solution was filtered to remove insoluble impurities. A second solution was prepared by dissolving 8.65 g of PhCOONa (60 mmol) in 100 mL H₂O. The two solutions were mixed and stirred for 30 min leading rapidly to the precipitation of a pink-orange powder. The product was isolated by vacuum filtration, it was then washed extensively with H₂O and was left to dry in air. Yield: 99.2% based on FeCl₃·6H₂O. IR (ATR): 3063 (w), 2164 (w), 1601 (m), 1560 (m), 1493 (w), 1400 (m), 1317 (w), 1177 (w), 1070 (w), 1024 (w), 1001 (w), 941 (w), 839 (w), 818 (w), 712 (m), 685 (m), 675 (m), 660 (w), 631 (m), 482 (m), 411 (w).

2.3. Physical Measurements for the Characterization of [Fe₃O(PhCO₂)₆(H₂O)₃]·PhCO₂

The IR spectrum of [Fe₃O(PhCO₂)₆(H₂O)₃]·PhCO₂ (Figure S1) was recorded on a Shimadzu FT/IR IRAffinity-1 spectrometer equipped with an ATR unit. Thermogravimetric analysis (TGA) was recorded on a Mettler-Toledo TGA/DSC1 instrument under a N₂ flow of 50 mL/min from room temperature to 800 °C with a heating rate of 10 °C min⁻¹. The powder X-ray diffraction pattern was recorded on a Bruker D8 Advance X-ray diffractometer (CuKα radiation, λ = 1.5418 Å). The particle size was calculated using an image taken on a Leica M205 C stereoscope equipped with a Leica DMC5400-20 Megapixel camera

(Figures S2 and S3). The image was taken from a sample of $[\text{Fe}_3\text{O}(\text{PhCO}_2)_6(\text{H}_2\text{O})_3]\cdot\text{PhCO}_2$, dispersed in water, on a glass slide.

The crystal structure of $[\text{Fe}_3\text{O}(\text{PhCO}_2)_6(\text{H}_2\text{O})_3]\cdot\text{PhCO}_2$ has never been reported by single-crystal x-ray diffraction since the product is formed as a polycrystalline powder, however, similar structures with the same trinuclear moiety, i.e., $[\text{Fe}_3\text{O}(\text{PhCOO}_2)_6(\text{H}_2\text{O})_3]^+$, exist in the literature (Table S1) [38–40]. Furthermore, to the best of our knowledge, the powder diffraction pattern of $[\text{Fe}_3\text{O}(\text{PhCO}_2)_6(\text{H}_2\text{O})_3]\cdot\text{PhCO}_2$ has never been reported. Herein, we manage to elucidate the structure of $[\text{Fe}_3\text{O}(\text{PhCO}_2)_6(\text{H}_2\text{O})_3]\cdot\text{PhCO}_2$ by applying the experimental X-ray powder diffraction data on a model treated by a simulated annealing method and refined with the Rietveld method (Figure 1, Tables S2 and S3) using EXPO 1.20.03 [41]. In order to create a suitable model, we examined all known $[\text{Fe}_3\text{O}(\text{PhCOO}_2)_6(\text{H}_2\text{O})_3]^+$ containing structures [38–40] from which we eliminated the solvates and replaced the counter anions with a PhCO_2^- , using the Avogadro 1.2.0 software [42]. The best results were acquired when we utilized the $[\text{Fe}_3\text{O}(\text{PhCOO}_2)_6(\text{H}_2\text{O})_3]^+$ cation from the crystal structure of $[\text{Fe}_3\text{O}(\text{PhCOO}_2)_6(\text{H}_2\text{O})_3]\text{NO}_3\cdot 3\text{MeCN}$ [38].

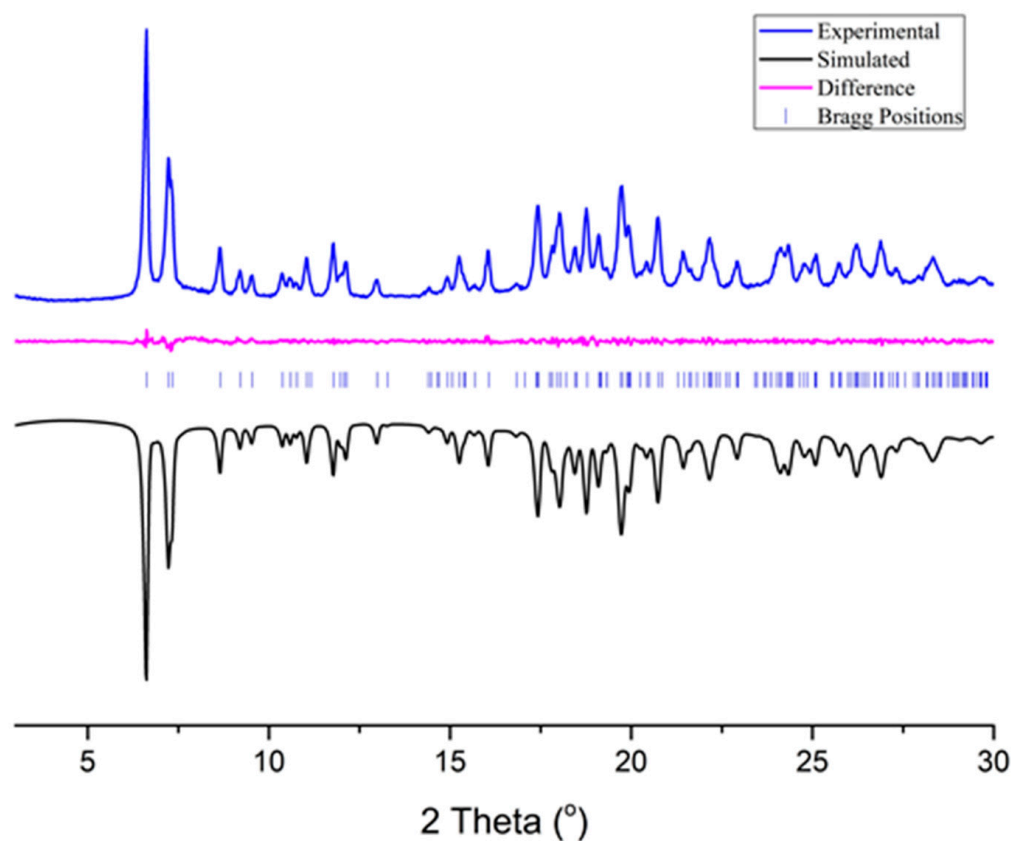


Figure 1. The final plot of the Rietveld refinement, showing the experimental, simulated (reverted) and difference powder diffraction patterns of $[\text{Fe}_3\text{O}(\text{PhCO}_2)_6(\text{H}_2\text{O})_3]\cdot\text{PhCO}_2$. Vertical markers refer to the calculated positions of the Bragg reflections (Table S4).

The structure of basic iron benzoate (Figure 2) consists of three Fe(III) cations bridged by a μ_3 -oxo bridge. Each pair of Fe(III) is bridged circumferentially by two benzoate anions through their carboxylate groups. Finally, the coordination sphere of each Fe(III) is completed by a terminal H_2O molecule (whose H atoms could not be modelled), and the total charge is balanced by a benzoate anion in the lattice.

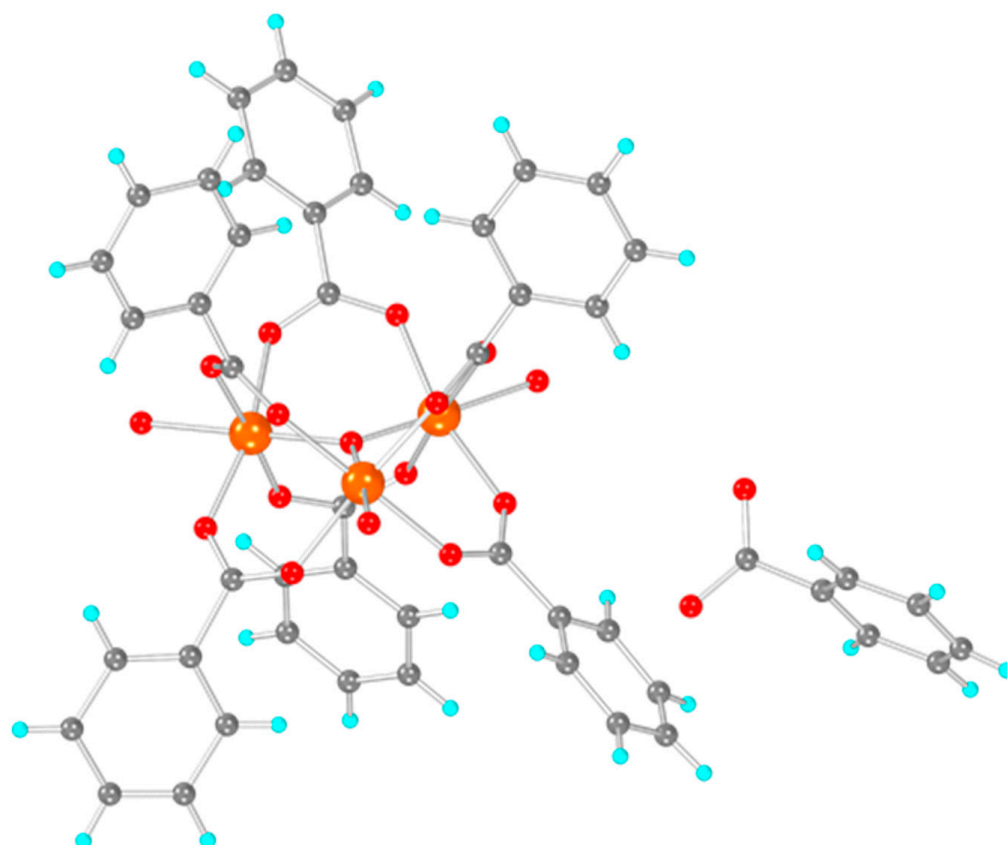


Figure 2. Structure of $[\text{Fe}_3\text{O}(\text{PhCO}_2)_6(\text{H}_2\text{O})_3]\cdot\text{PhCO}_2$ solved by powder X-ray diffraction. Colour code: Fe: orange, C: grey, H: turquoise, O: red.

Thermogravimetric analysis (TGA) (Figure S4) reveals that $[\text{Fe}_3\text{O}(\text{PhCO}_2)_6(\text{H}_2\text{O})_3]\cdot\text{PhCO}_2$ loses ~4.29% within the 25–137 °C temperature range, corresponding to the three coordinated H_2O molecules (their theoretical value is 4.98%). This is followed by a loss of ~10.63% within the 137–257 °C temperature range, corresponding to one benzoate anion (its theoretical value is 11.15%) and degrades immediately after that. The residue above 620 °C is 22.18% which corresponds to Fe_2O_3 (theoretical value 22.06%).

2.4. Fabrication of the 3D Printed Sensor Modified with Fe(III)-Cluster

The fabrication process of the 3D printed GLU sensor modified with Fe(III)-cluster is illustrated in Figure 3. The 3D printed electrode (3DPE) was designed with Tinkercad software and the printing conditions were set to 60 °C for the platform, 200 °C for the head dispenser, and 60 mm s^{-1} for the printing speed. Flashprint software was used for printing. The filament had a diameter of 1.75 mm and was PLA loaded with carbon black, and was obtained from Proto Pasta. For the construction of the GLU sensor, 10 μL of 6% (*w/v*) ethanolic mixture of $[\text{Fe}_3\text{O}(\text{PhCO}_2)_6(\text{H}_2\text{O})_3]\cdot\text{PhCO}_2$, was applied on the cyclic surface of the 3D printer and left for 5 min for its immobilization, followed by curing with an air stream from a gun for 1 extra min. Next, 10 μL of 1% (*w/v*) ethanolic solution of Nafion was added on the electrode cyclic surface and left to dry for 5 min. After that, the sensor was treated under an air stream for 1 min for complete drying.

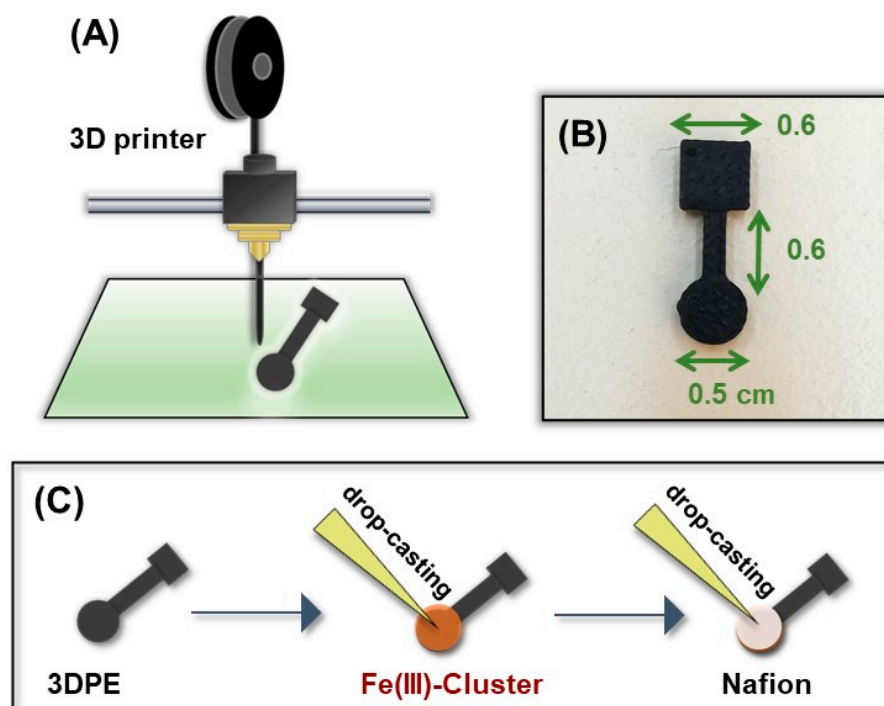


Figure 3. (A) Schematic illustration of the 3D printing process of the sensor. (B) A photograph of the 3D printed sensor and its dimensions in cm. (C) Schematic illustration of the drop-casting procedure for the construction of the GLU 3DPE modified with $[\text{Fe}_3\text{O}(\text{PhCO}_2)_6(\text{H}_2\text{O})_3]\cdot\text{PhCO}_2$.

2.5. Electrochemical Measurements

The electrochemical measurements were conducted in a 5 mL electrochemical cell in the presence of dissolved oxygen. The portable potentiostat was the EmStat3 (Palm Sens, Houten, The Netherlands) and operated by the PS Trace 4.2 software (Palm Sens, Houten, The Netherlands). The reference electrode was a saturated calomel electrode and the counter electrode was Pt wire. For the DPV measurements, a potential of -1.4 V for 360 s was applied on the 3D printed working electrode (WE), and then a scan (modulation amplitude, 50 mV; increment, 10 mV; pulse width, 75 ms; pulse repeat time, 50 ms) was run on the WE and the DPV response was recorded. The connection of the three electrodes to the portable potentiostat was accomplished using three crocodile clips.

3. Results and Discussion

3.1. Electrochemical Characterization of the 3D Printed Electrode Modified with $[\text{Fe}_3\text{O}(\text{PhCO}_2)_6(\text{H}_2\text{O})_3]\cdot\text{PhCO}_2$

Figure 4 depicts the DPV responses of the 3DPE modified with $[\text{Fe}_3\text{O}(\text{PhCO}_2)_6(\text{H}_2\text{O})_3]\cdot\text{PhCO}_2$ and the respective 3DPE modified with iron oxide towards $200 \mu\text{mol L}^{-1}$ GLU in PB (pH 4). The 3DPE modified with Fe(III)-cluster presented favorable performance offering a well-shaped DPV oxidation peak of GLU, while the respective 3DPE modified with iron oxide exhibited neglected response for GLU oxidation in these acidic conditions. It has been documented before that Fe_3O_4 , Fe_2O_3 , and FeOOH based electrodes require neutral or basic conditions in order to form Fe(III), which effectively catalyzed the oxidation of GLU [27–32]. The mechanism of electrocatalyzed oxidation of the GLU by the 3DPE modified with $[\text{Fe}_3\text{O}(\text{PhCO}_2)_6(\text{H}_2\text{O})_3]\cdot\text{PhCO}_2$ is based on the reduction of Fe(III) in the cluster to Fe(0) on the 3DPE surface, by setting a negative potential at -1.4 V for 360 s. Next, the metallic Fe(0) formed under this cathodic polarization process was oxidized to Fe(III) in the course of the scan potential from -1.4 V to $+1.5$ V. Finally, the in-situ electrogenerated Fe(III) oxidized GLU [27–32]. The whole mechanism is the following:

Mechanism:

(A) Electrogeneration of Fe(III):

Reduction: Fe(III)-Cluster \rightarrow Fe(0) (polarization of WE at -1.4 V for 360 s).

Oxidation: Fe(0) \rightarrow Fe(III) (DPV scan from -1.4 V to $+1.5$ V).

(B) Catalytic oxidation of GLU:

$2\text{Fe(III)} + \text{Glucose} \rightarrow 2\text{Fe(II)} + \text{Gluconolactone} + \text{H}_2\text{O}$.

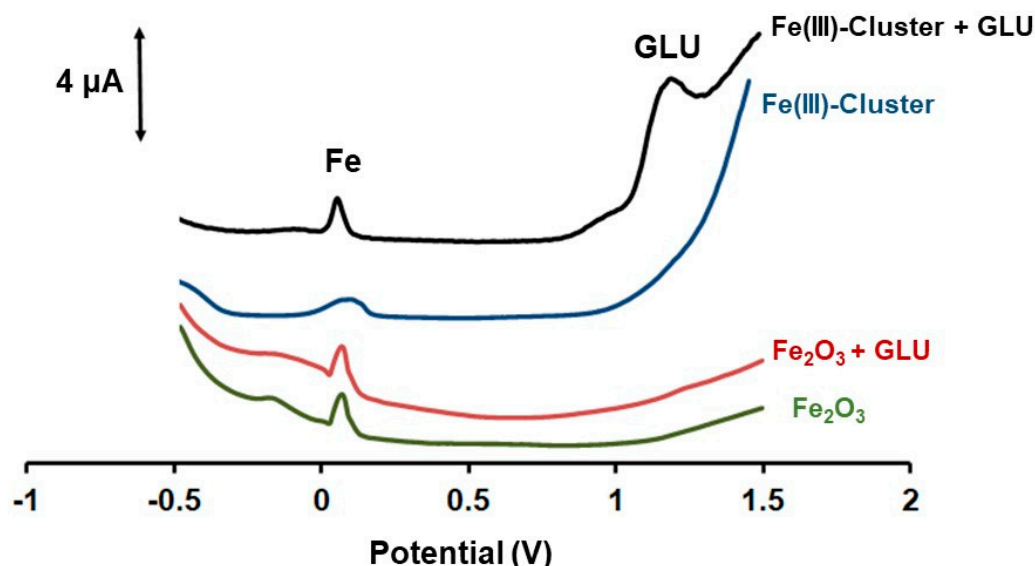


Figure 4. DPV responses of $\text{Fe}_3\text{O}(\text{PhCO}_2)_6(\text{H}_2\text{O})_3\cdot\text{PhCO}_2/3\text{DPE}$ and $\text{Fe}_3\text{O}_2/3\text{DPE}$ towards $200 \mu\text{mol L}^{-1}$ GLU in 0.1 mol L^{-1} PB (pH 4). The 3D printed sensor was modified with 6% *w/v* $\text{Fe}_3\text{O}(\text{PhCO}_2)_6(\text{H}_2\text{O})_3\cdot\text{PhCO}_2$ (blue and black lines) and with 6% *w/v* Fe_3O_2 (red and green lines) (both modifiers as ethanolic mixtures). The reduction potential was -1.4 V for 360 s for Fe(III)-Cluster, while the reduction time was 0 s in cases of iron oxide.

3.2. Effect of Reduction Time, Potential and Fe(III)-Cluster Loading on GLU Determination

The effect of the loading of the $\text{Fe}_3\text{O}(\text{PhCO}_2)_6(\text{H}_2\text{O})_3\cdot\text{PhCO}_2$ on the 3DPE surface, the reduction potential, and the reduction time of the 3DPE for the in-situ electrogeneration of Fe(III) were examined on the DPV response of $200 \mu\text{mol L}^{-1}$ GLU in 0.1 mol L^{-1} PB (pH 4) (Figure 5). Four loading levels of the $\text{Fe}_3\text{O}(\text{PhCO}_2)_6(\text{H}_2\text{O})_3\cdot\text{PhCO}_2$ on the 3DPE in the range 2–8% (*w/v*) (as ethanolic mixtures), step of 2%, were studied. As demonstrated in Figure 5, the $\text{Fe}_3\text{O}(\text{PhCO}_2)_6(\text{H}_2\text{O})_3\cdot\text{PhCO}_2/3\text{DPE}$ at 6% (*w/v*) yielded approximately 1.5 times higher voltammetric peak height of GLU than that of 4% and 2.5 higher than that of 2% (*w/v*) loadings, while its sensitivity was statistically comparable with that of 8% (*w/v*) loading. Hence, a $\text{Fe}_3\text{O}(\text{PhCO}_2)_6(\text{H}_2\text{O})_3\cdot\text{PhCO}_2/3\text{DPE}$ at 6% (*w/v*) loading was selected as the optimum, combining the minimal consumption of Fe(III)-cluster with the high DPV response of GLU in acidic conditions.

The effect of the reduction time and corresponding potential of the Fe(III)-cluster on the 3DPE surface was tested in the range 0 s to 480 s and from -1.6 V to 0.0 V, respectively. These parameters affect the quantity of the in-situ electrogenerated Fe(III) and, as a result, the catalytic electrocapability of the 3D printed sensor to GLU determination. As depicted in Figure 6A,B, the GLU oxidation responses increased with respect to the reduction period of time, while a sigmoidal shape is observed that shows a dependence on the reduction potentials. The GLU peak heights were low at more positive potentials, as these potential values were not adequately negative to establish the reduction of the Fe(III)-cluster to metallic Fe(0) on the WE surface. At more negative potentials, the deposition of Fe(0) on 3DPE was favored and the peak currents of GLU increased rapidly up to -1.4 V, where it leveled-off. For the further experiments, a reduction potential of -1.4 V for 360 s was

selected, as this presented a satisfactory compromise between high sensitivity and short analysis times.

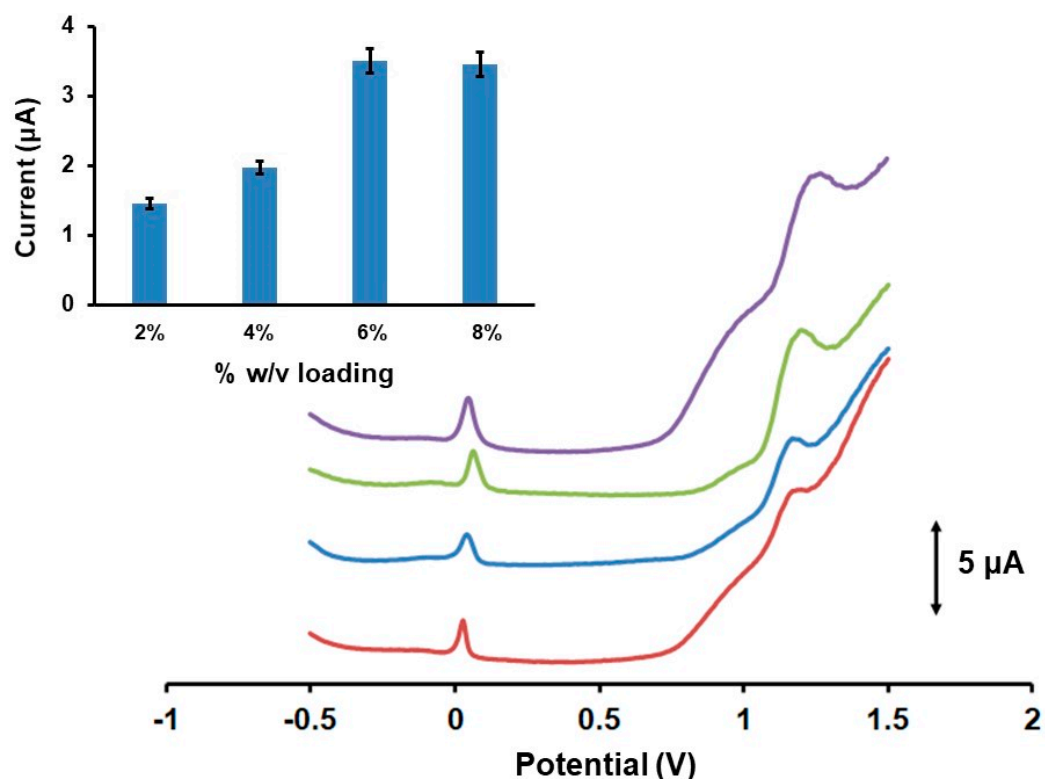


Figure 5. Effect of the concentration of the $\text{Fe}_3\text{O}(\text{PhCO}_2)_6(\text{H}_2\text{O})_3]\cdot\text{PhCO}_2$ at the 3DPE on the DPV peak current values of $200 \mu\text{mol L}^{-1}$ GLU in 0.1 mol L^{-1} PB (pH 4) and the respective DPV responses (from down to up 2, 4, 6, 8% (*w/v*)). Each bar is the mean value \pm SD ($n = 3$). Reduction of Fe(III)-cluster at -1.4 V for 360 s.

3.3. Analytical Features of 3D Printed GLU Sensor

Figure 7 presents the DPV responses and the calibration plot of GLU on the $\text{Fe}_3\text{O}(\text{PhCO}_2)_6(\text{H}_2\text{O})_3]\cdot\text{PhCO}_2/3\text{DPE}$ in the concentration range of 25 to $500 \mu\text{mol L}^{-1}$ in 0.1 mol L^{-1} PB (pH 4). The voltammetric response of the 3D printed sensor to GLU oxidation increased linearly with increasing GLU concentration, with a correlation coefficient of 0.998, and the calibration curve fell within the physiological levels of GLU secreted in human sweat [12]. The limit of detection (LOD) was calculated by the equation $\text{LOD} = 3 s_y/a$, where s_y is the standard deviation of the y-residuals of the calibration plot, and a is the slope of the calibration, which was $4.3 \mu\text{mol L}^{-1}$. The LOD of GLU achieved with the $\text{Fe}_3\text{O}(\text{PhCO}_2)_6(\text{H}_2\text{O})_3]\cdot\text{PhCO}_2/3\text{DPE}$ in acidic sweat conditions compares well with those achieved with other iron-based enzyme-free electrodes operated in neutral and basic media [28–32] (Table 1). The within-sensor reproducibility (stated as the % relative standard deviation (RSD) of ten repetitive responses at the 3DPE) was 4.8% for GLU and the between-sensor reproducibility (expressed as the % RSD at six different 3DPEs) was 8.1% (both at the $250 \mu\text{mol L}^{-1}$ GLU level), revealing high precision of the modified 3DPEs responses.

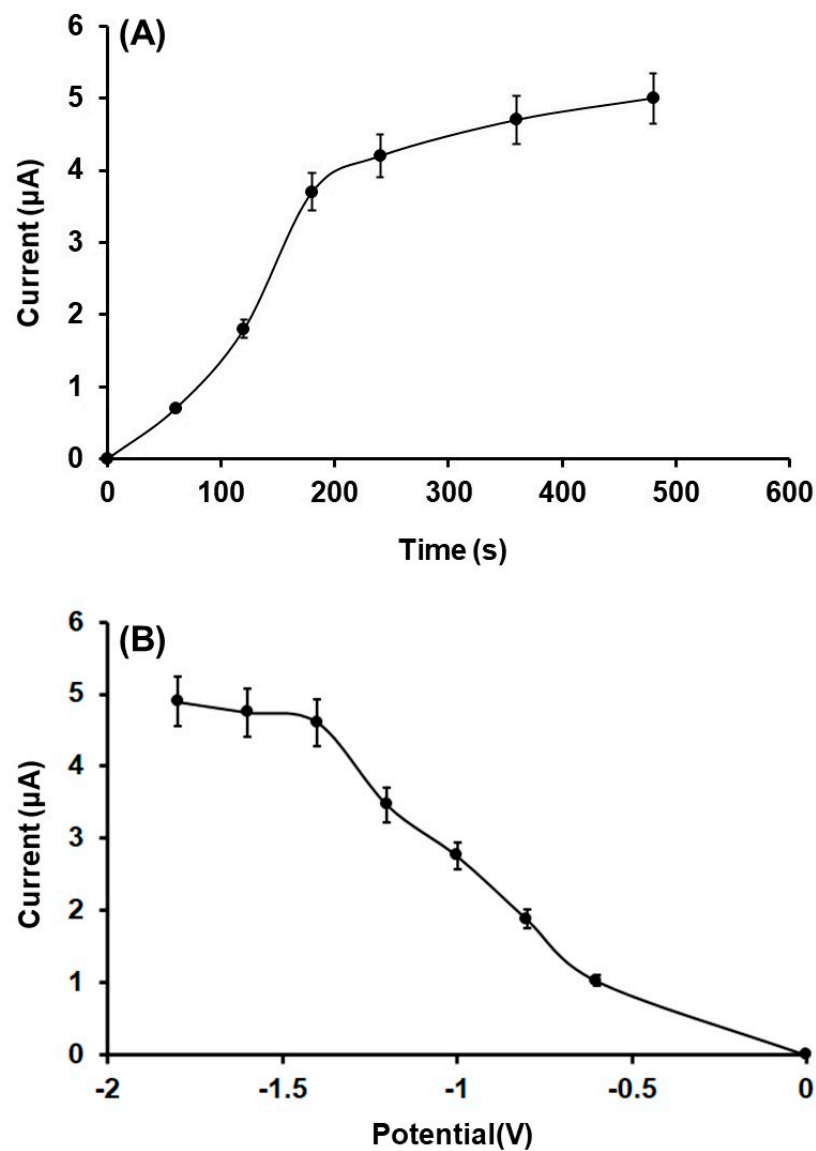


Figure 6. (A) Effect of the reduction time on the DPV peak current values of $250 \mu\text{mol L}^{-1}$ GLU in 0.1 mol L^{-1} PB (pH 4) obtained with $\text{Fe}_3\text{O}(\text{PhCO}_2)_6(\text{H}_2\text{O})_3 \cdot \text{PhCO}_2/3\text{DPE}$ applying a reduction potential at -1.4 V . (B) Effect of the reduction potential on the DPV peak currents of $250 \mu\text{mol L}^{-1}$ GLU in 0.1 mol L^{-1} PB (pH 4) at $\text{Fe}_3\text{O}(\text{PhCO}_2)_6(\text{H}_2\text{O})_3 \cdot \text{PhCO}_2/3\text{DPE}$ under 360 s reduction time. Each point is the mean value \pm SD ($n = 3$).

Table 1. Performance comparison of various iron-based nonenzymatic glucose sensors.

Electrode	Modifier	Operation Media (pH)	LOD ($\mu\text{mol L}^{-1}$)	Ref.
Glassy carbon	Fe_2O_3	PB (pH 7.5)	0.6	[28]
Glassy carbon	Fe_2O_3	PB (pH 7.5)	6.0	[29]
Glassy carbon	Fe_3O_4	PB (pH 7.0)	15.0	[30]
Iron foil	Fe_3O_4	NaOH (pH 13.0)	0.1	[31]
Glassy carbon	FeOOH	PB (pH 7.4)	7.8	[32]
3D-CB/PLA	$\text{Fe}_3\text{O}(\text{PhCO}_2)_6(\text{H}_2\text{O})_3 \cdot \text{PhCO}_2$	PB (pH 4.0)	4.3	This work

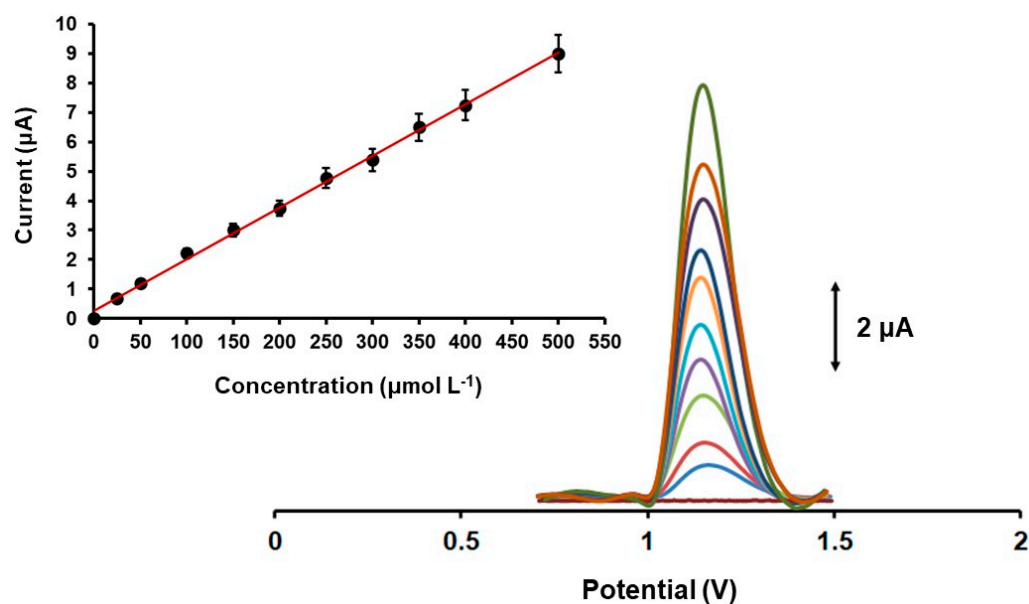


Figure 7. Baseline-corrected DPV responses of GLU concentrations in the range 0–500 $\mu\text{mol L}^{-1}$ (from down to up: 0, 25, 50, 100, 150, 200, 250, 300, 350, 400, 500 $\mu\text{mol L}^{-1}$ GLU) in 0.1 mol L^{-1} PB (pH 4) applying a reduction potential at -1.4 V for 360 s. Each point in the calibration plots is the mean value \pm SD ($n = 3$).

3.4. Interference Study

For enzyme-free GLU sensors, selectivity is a key factor for their noninvasive applications, as the sensors can be subject to interferences by other biomarkers (such as urea, uric acid, and lactic acid) co-existing in sweat that can impact the precision of GLU monitoring. To examine the selectivity of $\text{Fe}_3\text{O}(\text{PhCO}_2)_6(\text{H}_2\text{O})_3 \cdot \text{PhCO}_2/3\text{DPE}$ in sweat, a concentration of 220 mmol L^{-1} urea, 250 $\mu\text{mol L}^{-1}$ uric acid, and 55 mmol L^{-1} lactic acid was added separately and together in the artificial sweat, and their effect on the DPV oxidation peak of 200 $\mu\text{mol L}^{-1}$ GLU was studied [12,43]. As shown in Figure 8A the sweat biomarkers did not cause any statistically significant effect on the DPV GLU oxidation peak, demonstrating the satisfactory selectivity 3D printed GLU sensor to other common co-existing biomarkers in sweat.

3.5. Application to Artificial Sweat

In order to assess the applicability of the enzyme-free method in noninvasive bioanalysis, three artificial sweat samples containing 120 $\mu\text{mol L}^{-1}$ (Figure 8B), 200 and 300 $\mu\text{mol L}^{-1}$ GLU were measured by $\text{Fe}_3\text{O}(\text{PhCO}_2)_6(\text{H}_2\text{O})_3 \cdot \text{PhCO}_2/3\text{DPE}$ s. The artificial sweat was composed of 3 mmol L^{-1} NH_4Cl , 50 $\mu\text{mol L}^{-1}$ MgCl_2 , 0.4 mmol L^{-1} CaCl_2 , 80 mmol L^{-1} NaCl , 8 mmol L^{-1} KCl , 25 $\mu\text{mol L}^{-1}$ uric acid, 22 mmol L^{-1} urea, and 5.5 mmol L^{-1} lactic acid [12]. The standard addition method was applied for the determination of GLU in the sweat samples, calculating the respective recovery values. Satisfactory recoveries values for GLU were obtained ranging from 97 to 102%. These results demonstrate the accuracy of the 3D printed sensor modified with Fe(III)-cluster to sensitive and selective monitoring of GLU in sweat conditions.

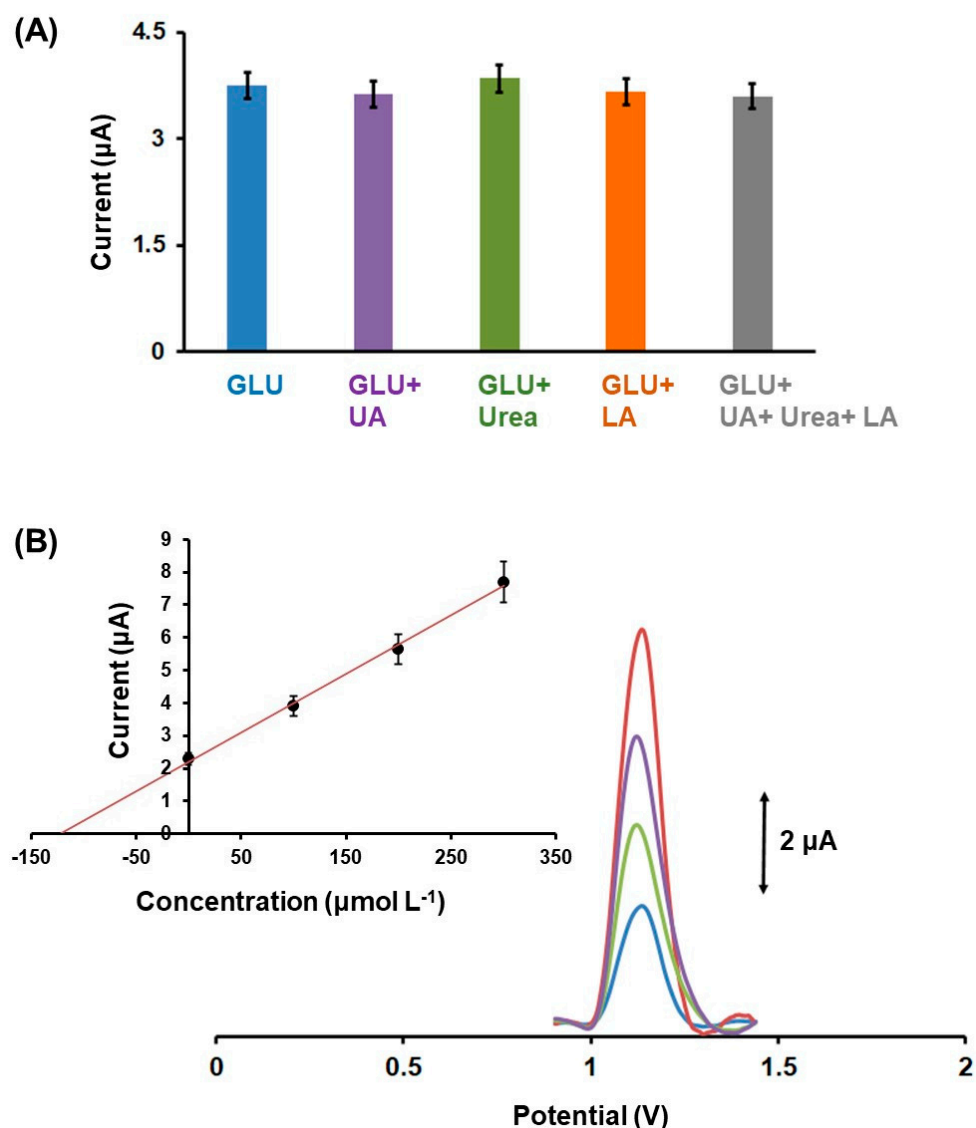


Figure 8. (A) Effect of different biomarkers presented in sweat on the DPV peak height of $200 \mu\text{mol L}^{-1}$ GLU at the $\text{Fe}_3\text{O}(\text{PhCO}_2)_6(\text{H}_2\text{O})_3\text{]}\cdot\text{PhCO}_2/3\text{DPE}$, where: (blue bar) $200 \mu\text{mol L}^{-1}$ GLU in artificial sweat (AS); (purple bar) $200 \mu\text{mol L}^{-1}$ GLU + $250 \mu\text{mol L}^{-1}$ UA in AS; (green bar) $200 \mu\text{mol L}^{-1}$ GLU + 220mmol L^{-1} urea in AS; (orange bar) $200 \mu\text{mol L}^{-1}$ GLU + 55mmol L^{-1} lactic acid (LA) in AS; (grey bar) $200 \mu\text{mol L}^{-1}$ GLU + $250 \mu\text{mol L}^{-1}$ UA + 220mmol L^{-1} urea + 55mmol L^{-1} lactic acid in AS. (B) DPV responses and respective plot for the determination of GLU in an artificial sweat sample spiked with $120 \mu\text{mol L}^{-1}$ GLU. Each point in the bar and in the standard addition plots is the mean value \pm SD ($n = 3$).

4. Conclusions

In this work, we have developed a new type of 3D printed sensor modified with water-stable $\text{Fe}_3\text{O}(\text{PhCO}_2)_6(\text{H}_2\text{O})_3\text{]}\cdot\text{PhCO}_2$ for enzyme-free GLU monitoring in acidic epidermal sweat environment. The Fe(III)-cluster served as a Fe(III) precursor used in the electrocatalytic oxidation of GLU. The 3D printed sensor presented favorable electroanalytical action in the DPV selective determination of GLU, offering satisfactory reproducibility and very low LOD. These features combined with 3D printing technology set the presented sensor as an innovative addition to the arena of electrochemical transducers used for noninvasive bioapplications.

Supplementary Materials: The following supporting information can be downloaded at: <https://www.mdpi.com/article/10.3390/bios12121156/s1>, Table S1: The reported crystal structures containing the $[\text{Fe}_3\text{O}(\text{PhCOO}_2)_6(\text{H}_2\text{O})_3]^+$ moiety; Table S2: Crystal data and structure refinement for $[\text{Fe}_3\text{O}(\text{PhCO}_2)_6(\text{H}_2\text{O})_3]\cdot\text{PhCO}_2$; Table S3: Atomic coordinates ($\times 10^4$) and equivalent isotropic displacement parameters ($\text{\AA}^2 \times 10^3$) for $[\text{Fe}_3\text{O}(\text{PhCO}_2)_6(\text{H}_2\text{O})_3]\cdot\text{PhCO}_2$; Table S4: List of Bragg positions (shown as blue dashes in Figure 1) from the Rietveld Analysis of $[\text{Fe}_3\text{O}(\text{PhCO}_2)_6(\text{H}_2\text{O})_3]\cdot\text{PhCO}_2$; Figure S1: The IR spectrum (ATR) of $[\text{Fe}_3\text{O}(\text{PhCO}_2)_6(\text{H}_2\text{O})_3]\cdot\text{PhCO}_2$ in the $450\text{--}4000\text{ cm}^{-1}$ range; Figure S2: Image of $[\text{Fe}_3\text{O}(\text{PhCO}_2)_6(\text{H}_2\text{O})_3]\cdot\text{PhCO}_2$ dispersed in water on a glass slide; Figure S3: Histogram of particle sizes ranging between 50 and 230 μm (black bars), and Gaussian fit (red line); Figure S4: Thermogravimetric analysis (TGA) graph of $[\text{Fe}_3\text{O}(\text{PhCO}_2)_6(\text{H}_2\text{O})_3]\cdot\text{PhCO}_2$ in the $25\text{--}800\text{ }^\circ\text{C}$ temperature range. Reference [44] is cited in the supplementary materials.

Author Contributions: Conceptualization, C.K. and G.S.P. investigation, E.K. and A.K.P.; resources, C.K., A.E., G.S.P. and N.T.; writing—original draft preparation, C.K.; writing—review and editing, C.K.; visualization, C.K.; supervision, C.K. and G.S.P. All authors have read and agreed to the published version of the manuscript.

Funding: This research has been co-financed by the European Regional Development Fund of the European Union and Greek national funds through the Operational Program Competitiveness, Entrepreneurship and Innovation, under the call RESEARCH-CREATE-INNOVATE (project code: T2EDK-00028/MIS 5067540).

Institutional Review Board Statement: Not applicable.

Informed Consent Statement: Not applicable.

Conflicts of Interest: The authors declare no conflict of interest.

References

1. Whiting, D.R.; Guariguata, L.; Weil, C.; Shaw, J. IDF Diabetes Atlas: Global estimates of the prevalence of diabetes for 2011 and 2030. *Diabetes Res. Clin. Pract.* **2011**, *94*, 311–321. [\[CrossRef\]](#)
2. Karpova, E.V.; Karyakin, A.A. Noninvasive monitoring of diabetes and hypoxia by wearable flow-through biosensors. *Curr. Opin. Electrochem.* **2020**, *23*, 16–20. [\[CrossRef\]](#)
3. Kim, J.; Campbell, A.S.; de Ávila, B.E.F.; Wang, J. Wearable biosensors for healthcare monitoring. *Nat. Biotechnol.* **2019**, *37*, 389–406. [\[CrossRef\]](#)
4. Karpova, E.V.; Karyakina, E.E.; Karyakin, A.A. Wearable non-invasive monitors of diabetes and hypoxia through continuous analysis of sweat. *Talanta* **2020**, *215*, 120922. [\[CrossRef\]](#)
5. Bandodkar, A.J.; Jeang, W.J.; Ghaffari, R.; Rogers, J.A. Wearable Sensors for Biochemical Sweat Analysis. *Annu. Rev. Anal. Chem.* **2019**, *12*, 1–22. [\[CrossRef\]](#)
6. Zhu, B.; Li, X.; Zhou, L.; Su, B. An Overview of Wearable and Implantable Electrochemical Glucose Sensors. *Electroanalysis* **2022**, *34*, 237–245. [\[CrossRef\]](#)
7. Peng, Z.; Xie, X.; Tan, Q.; Kang, H.; Cui, J.; Zhang, X.; Li, W.; Feng, G. Blood glucose sensors and recent advances: A review. *J. Innov. Opt. Health Sci.* **2022**, *15*, 2230003. [\[CrossRef\]](#)
8. Ma, R.; Shao, R.; An, X.; Zhang, Q.; Sun, S. Recent advancements in noninvasive glucose monitoring and closed-loop management systems for diabetes. *J. Mater. Chem. B* **2022**, *10*, 5537–5555. [\[CrossRef\]](#)
9. Garcia-Garcia, F.J.; Salazar, P.; Yubero, F.; González-Elipe, A.R. Non-enzymatic Glucose electrochemical sensor made of porous NiO thin films prepared by reactive magnetron sputtering at oblique angles. *Electrochim. Acta* **2016**, *201*, 38–44. [\[CrossRef\]](#)
10. Salimi, A.; Roushani, M. Non-enzymatic glucose detection free of ascorbic acid interference using nickel powder and nafion sol-gel dispersed renewable carbon ceramic electrode. *Electrochem. Commun.* **2005**, *7*, 879–887. [\[CrossRef\]](#)
11. Zhu, X.; Ju, Y.; Chen, J.; Liu, D.; Liu, H. Nonenzymatic wearable sensor for electrochemical analysis of perspiration glucose. *ACS Sens.* **2018**, *3*, 1135–1141. [\[CrossRef\]](#) [\[PubMed\]](#)
12. Katseli, V.; Economou, A.; Kokkinos, C. Smartphone-Addressable 3D-Printed Electrochemical Ring for Nonenzymatic Self-Monitoring of Glucose in Human Sweat. *Anal. Chem.* **2021**, *93*, 3331–3336. [\[CrossRef\]](#) [\[PubMed\]](#)
13. Naikoo, G.A.; Salim, H.; Hassan, I.U.; Awan, T.; Arshad, F.; Pedram, M.Z.; Ahmed, W.; Qurashi, A. Recent Advances in Non-Enzymatic Glucose Sensors Based on Metal and Metal Oxide Nanostructures for Diabetes Management—A Review. *Front. Chem.* **2021**, *9*, 748957. [\[CrossRef\]](#) [\[PubMed\]](#)
14. Thatikayala, D.; Ponnamma, D.; Sadasivuni, K.K.; Cabibihan, J.J.; Al-Ali, A.K.; Malik, R.A.; Min, B. Progress of Advanced Nanomaterials in the Non-Enzymatic Electrochemical Sensing of Glucose and H_2O_2 . *Biosensors* **2020**, *10*, 151. [\[CrossRef\]](#)

15. Yuan, K.; Zhang, Y.; Huang, S.; Yang, S.; Zhao, S.; Liu, F.; Peng, Q.; Zhao, Y.; Zhang, G.; Fan, J.; et al. Copper Nanoflowers on Carbon Cloth as a Flexible Electrode toward Both Enzymeless Electrocatalytic Glucose and H₂O₂. *Electroanalysis* **2021**, *33*, 1800–1809. [[CrossRef](#)]
16. Hu, Q.; Qin, J.; Wang, X.F.; Ran, G.Y.; Wang, Q.; Liu, G.X.; Ma, J.P.; Ge, J.Y.; Wang, H.Y. Cu-Based Conductive MOF Grown in situ on Cu Foam as a Highly Selective and Stable Non-Enzymatic Glucose Sensor. *Front. Chem.* **2021**, *9*, 786970. [[CrossRef](#)]
17. Yang, S.; Wang, Y.; Sheng, Q. Heterostructural NiCo₂O₄ Nanocomposites for Nonenzymatic Electrochemical Glucose Sensing. *Electroanalysis* **2022**, *34*, 835–843. [[CrossRef](#)]
18. Lu, Y.; Jiang, B.; Fang, L.; Fan, S.; Wu, F.; Hu, B.; Meng, F.M. Highly Sensitive Nonenzymatic Glucose Sensor Based on 3D Ultrathin NiFe Layered Double Hydroxide Nanosheets. *Electroanalysis* **2017**, *29*, 1755–1761. [[CrossRef](#)]
19. Liu, S.; Jiang, X.; Waterhouse, G.I.N.; Zhang, Z.M.; Yu, L. min A Cu₂O/PEDOT/graphene-modified electrode for the enzyme-free detection and quantification of glucose. *J. Electroanal. Chem.* **2021**, *897*, 115558. [[CrossRef](#)]
20. Guati, C.; Gomez-Coma, L.; Fallanza, M.; Ortiz, I. Non-enzymatic amperometric glucose screen-printed sensors based on copper and copper oxide particles. *Appl. Sci.* **2021**, *11*, 10830. [[CrossRef](#)]
21. Fang, L.; Cai, Y.; Huang, B.; Cao, Q.; Zhu, Q.; Tu, T.; Ye, X.; Liang, B. A highly sensitive nonenzymatic glucose sensor based on Cu/Cu₂O composite nanoparticles decorated single carbon fiber. *J. Electroanal. Chem.* **2021**, *880*, 114888. [[CrossRef](#)]
22. Gao, W.; Zhou, X.; Heinig, N.F.; Thomas, J.P.; Zhang, L.; Leung, K.T. Nonenzymatic Saliva-Range Glucose Sensing Using Electrodeposited Cuprous Oxide Nanocubes on a Graphene Strip. *ACS Appl. Nano Mater.* **2021**, *4*, 4790–4799. [[CrossRef](#)]
23. Liu, C.; Xue, K.; Sun, A.; Chen, D.; Zhang, P.; Cui, G. Cu₂O ordered nanoarrays for non-enzymatic glucose detection. *J. Appl. Sci. Eng.* **2021**, *24*, 829–835. [[CrossRef](#)]
24. Lin, W.J.; Lin, Y.S.; Chang, H.T.; Unnikrishnan, B.; Huang, C.C. Electrocatalytic CuBr@CuO nanoparticles based salivary glucose probes. *Biosens. Bioelectron.* **2021**, *194*, 113610. [[CrossRef](#)] [[PubMed](#)]
25. Alam, M.M.; Howlader, M.M.R. Nonenzymatic electrochemical sensors via Cu native oxides (CuNO_x) for sweat glucose monitoring. *Sens. Bio-Sens. Res.* **2021**, *34*, 100453. [[CrossRef](#)]
26. Redondo, E.; Pumera, M. Fully metallic copper 3D-printed electrodes via sintering for electrocatalytic biosensing. *Appl. Mater. Today* **2021**, *25*, 100453. [[CrossRef](#)]
27. Neravathu, D.; Paloly, A.R.; Sajan, P.; Satheesh, M.; Bushiri, M.J. Hybrid nanomaterial of ZnFe₂O₄/α-Fe₂O₃ implanted graphene for electrochemical glucose sensing application. *Diam. Relat. Mater.* **2020**, *106*, 107852. [[CrossRef](#)]
28. Chen, Y.; Zhang, H.; Xue, H.; Hu, X.; Wang, G.; Wang, C. Construction of a non-enzymatic glucose sensor based on copolymer P4VP-co-PAN and Fe₂O₃ nanoparticles. *Mater. Sci. Eng. C* **2014**, *35*, 420–425. [[CrossRef](#)]
29. Cao, X.; Wang, N. A novel non-enzymatic glucose sensor modified with Fe₂O₃ nanowire arrays. *Analyst* **2011**, *136*, 4241–4246. [[CrossRef](#)]
30. Masoomi-Godarzi, S.; Khodadadi, A.A.; Vesali-Naseh, M.; Mortazavi, Y. Highly Stable and Selective Non-Enzymatic Glucose Biosensor Using Carbon Nanotubes Decorated by Fe₃O₄ Nanoparticles. *J. Electrochem. Soc.* **2014**, *161*, B19–B25. [[CrossRef](#)]
31. Zhang, C.; Ni, H.; Chen, R.; Zhan, W.; Zhang, B.; Lei, R.; Xiao, T.; Zha, Y. Enzyme-free glucose sensing based on Fe₃O₄ nanorod arrays. *Microchim. Acta* **2015**, *182*, 1811–1818. [[CrossRef](#)]
32. Xia, C.; Ning, W. A novel non-enzymatic electrochemical glucose sensor modified with FeOOH nanowire. *Electrochem. Commun.* **2010**, *12*, 1581–1584. [[CrossRef](#)]
33. Carrasco-Correa, E.J.; Simó-Alfonso, E.F.; Herrero-Martínez, J.M.; Miró, M. The emerging role of 3D printing in the fabrication of detection systems. *TrAC-Trends Anal. Chem.* **2021**, *136*, 116177. [[CrossRef](#)]
34. Abdalla, A.; Patel, B.A. 3D-printed electrochemical sensors: A new horizon for measurement of biomolecules. *Curr. Opin. Electrochem.* **2020**, *20*, 78–81. [[CrossRef](#)]
35. Omar, M.H.; Razak, K.A.; Ab Wahab, M.N.; Hamzah, H.H. Recent progress of conductive 3D-printed electrodes based upon polymers/carbon nanomaterials using a fused deposition modelling (FDM) method as emerging electrochemical sensing devices. *RSC Adv.* **2021**, *11*, 16557–16571. [[CrossRef](#)] [[PubMed](#)]
36. Ambrosi, A.; Bonanni, A. How 3D printing can boost advances in analytical and bioanalytical chemistry. *Microchim. Acta* **2021**, *188*, 265. [[CrossRef](#)]
37. Earnshaw, A.; Figgis, B.N.; Lewis, J. Chemistry of polynuclear compounds. Part VI. Magnetic properties of trimeric chromium and iron carboxylates. *J. Chem. Soc. A Inorg. Phys. Theor.* **1966**, 1656–1663. [[CrossRef](#)]
38. Psycharis, V.; Raptopoulou, C.P.; Boudalis, A.K.; Sanakis, Y.; Fardis, M.; Diamantopoulos, G.; Papavassiliou, G. Syntheses, Structural, and Physical Studies of Basic Cr III and Fe III Benzilates and Benzoates: Evidence of Antisymmetric Exchange and Distributions of Isotropic and Antisymmetric Exchange Parameters. *Eur. J. Inorg. Chem.* **2006**, *2006*, 3710–3723. [[CrossRef](#)]
39. Georgopoulou, A.N.; Sanakis, Y.; Psycharis, V.; Raptopoulou, C.P.; Boudalis, A.K. Mössbauer spectra of two extended series of basic iron(III) carboxylates [Fe₃O(O₂CR)₆(H₂O)₆]A (A⁻ = ClO₄⁻, NO₃⁻). *Hyperfine Interact.* **2010**, *198*, 229–241. [[CrossRef](#)]
40. Cadelnic, I.; Shova, S.; Simonov, Y.A.; Cendrowska, E.; Gdaniec, M.; Jovmir, T.; Turta, C.; Bulhac, I. Crystal and molecular structure of [Fe₃O(C₆H₅COO)₆(H₂O)₃]·3-Cl-PyH·(CH₃C₆H₄SO₃)₂·2H₂O. *Pol. J. Chem.* **1997**, *71*, 501–508.
41. Altomare, A.; Cuocci, C.; Giacobozzo, C.; Moliterni, A.; Rizzi, R.; Corriero, N.; Falcicchio, A. EXPO2013: A kit of tools for phasing crystal structures from powder data. *J. Appl. Crystallogr.* **2013**, *46*, 1231–1235. [[CrossRef](#)]

42. Hanwell, M.D.; Curtis, D.E.; Lonie, D.C.; Vandermeersch, T.; Zurek, E.; Hutchison, G.R. Avogadro: An advanced semantic chemical editor, visualization, and analysis platform. *J. Cheminform.* **2012**, *4*, 17. [[CrossRef](#)] [[PubMed](#)]
43. Vasiliou, F.; Plessas, A.K.; Economou, A.; Thomaidis, N.; Papaefstathiou, G.S.; Kokkinos, C. Graphite paste sensor modified with a Cu(II)-complex for the enzyme-free simultaneous voltammetric determination of glucose and uric acid in sweat. *J. Electroanal. Chem.* **2022**, *917*, 116393. [[CrossRef](#)]
44. Schneider, C.A.; Rasband, W.S.; Eliceiri, K.W. NIH Image to ImageJ: 25 years of image analysis. *Nat. Methods* **2012**, *9*, 671–675. [[CrossRef](#)] [[PubMed](#)]